

Highlights

Sub-surface granular dynamics in the context of oblique, low-velocity impacts into angular granular media

Peter M. Miklavčič, Hesam Askari, Paul Sánchez, Alice C. Quillen, Esteban Wright

- Finite element methods support modeling of impacts into discrete triangular grains
- Simulations reproduce experimental ricochet, roll-out, and full-stop behaviors of projectile
- Visualization of local grain packing reveals breadth of granular disturbance from impact
- Strain distributions reveal zones of perturbed media around the crater
- Higher velocity impacts spur increasingly lateral granular dissipative mechanisms

Sub-surface granular dynamics in the context of oblique, low-velocity impacts into angular granular media

Peter M. Miklavčič^{a,*}, Hesam Askari^a, Paul Sánchez^b, Alice C. Quillen^c and Esteban Wright^c

^aDepartment of Mechanical Engineering, University of Rochester, 235 Hopeman Building, P.O. Box 270132, Rochester, NY, 14627, USA

^bColorado for Astrodynamics Research, University of Colorado Boulder, 3775 Discovery Dr., Boulder, CO, 80303, USA

^cDepartment of Physics and Astronomy, University of Rochester, 206 Bausch and Lomb Hall, P.O. Box 270171, Rochester, NY, 14627, USA

ARTICLE INFO

Keywords:
collisional physics
cratering
impact processes
regoliths


ABSTRACT

Oblique, low-velocity impacts onto extraterrestrial terrain are an inevitable occurrence during space exploration. We conduct two-dimensional discrete simulations to model such impacts into a bed of triangular grains. Finite element method provides the basis for simulation, enabling the angular grain geometry. Our findings re-create the three classes of impact behavior previously noted from experiments: full-stop, rollout, and ricochet (Wright, Quillen, South, Nelson, Sánchez, Siu, Askari, Nakajima and Schwartz, 2020). An application of Set Voronoi tessellation assesses packing fraction at a high resolution, revealing how grains shift relative to each other during an impact event. Calculation of Von Mises strain distributions then reveal how grains shift relative to the overall system, leading to the notion of the 'skin zone'. Intuition would suggest that the region of perturbed grains would grow deeper with higher velocity impacts, results instead show that increasing velocity may actually evoke a change in the grains' dissipative response that boosts lateral perturbation. Finally, we consider as a whole how sub-surface response could link with impactor dynamics to deepen our understanding of oblique, low-velocity impact events and help to improve mission outcomes.

1. Introduction

In recent decades, navigation of extraterrestrial (ET) terrain has presented a new front to the field of granular mechanics. Such environments differ from Earth because of different levels of gravity, low atmospheric pressure and materials that differ from those commonly found on Earth. The asteroid is one such environment of interest. The population of Near-Earth-Asteroids (NEAs) within reach of spacecraft are theorized to be composed entirely of rubble (Burns, 1975; Pravec and Harris, 2000; Walsh, 2018). These asteroids form over time by accretion of fragments of rock held together by self-gravity, a process that has spurred simulation research of its own (Leinhardt et al., 2000; Bagatin et al., 2001; Michel et al., 2002; Richardson et al., 2005; Sánchez and Scheeres, 2011; Sánchez and Scheeres, 2014; Sánchez, 2015; Ferrari et al., 2019; Ferrari and Tanga, 2020; Michel et al., 2020; Sánchez et al., 2021). Missions to these asteroids have returned images and even samples of the surface asteroid material, offering insight into the harsh environments that spacecraft must inevitably endure (Yano et al., 2006; Tsuchiyama et al., 2011; Nakamura et al., 2011; Watanabe et al., 2017).

Low velocity impacts on extraterrestrial surfaces have been subject of limited interest in the literature. Nonetheless, future exploration missions - to moons, planets, or asteroids - will likely encounter landings upon a rubble or regolith surface, making study of such impacts important for mission preparedness. The MASCOT lander touching down on asteroid Ryugu underlines this importance, as it has become the subject of simulations studying the impact at the landing site (Thuillet, Florian et al., 2018, 2021). Other literature studies the populations of craters observed on a planet's or asteroid's surface (Gou et al., 2018) focusing on such metrics as the depth-to-diameter ratio (Noguchi et al., 2021). Morphometry of craters have been connected through various scaling research (Goldman and Umbanhowar, 2008; Dowling and Dowling, 2013). The space shuttle and parabolic test flights have also supported experimental campaigns for studying low-velocity normal impacts into regolith simulant (Brisset et al., 2018). Oblique impacts have been less well studied experimentally, though recently Wright et al. studied impacts of a marble into sand and gravel as a function of impact angle and velocity, classifying resultant behavior into categories dependent upon whether the

 pmiklavc@ur.rochester.edu (P.M. Miklavčič); askari@rochester.edu (H. Askari); diego.sanchez-lana@colorado.edu (P. Sánchez); alice.quillen@rochester.edu (A.C. Quillen); ewrig15@ur.rochester.edu (E. Wright)
ORCID(s): 0000-0002-9724-8744 (P.M. Miklavčič)

projectile ricocheted off the media or not (Wright et al., 2020, 2021). This body of work provides valuable information about the surface and overall impactor behavior in low velocity impact conditions, but the dynamics of sub-surface grains and how these correspond to the impact dynamics are rarely studied.

Discrete element simulations offer great potential for studying sub-surface dynamics, though such methods are constrained by how accurately and efficiently each grain and its local interactions are modeled. A standard approach is to assume a spherical grain geometry which enables streamlined algorithms for contact detection and response (Cundall and Strack, 1979). Nonetheless, grain geometries are never perfectly round. This could not be more true for regolith, where grains are rougher than Earthen quartz sands due to an absence of erosive forces such as water and atmosphere. Regolith also behaves differently than quartz sands. Under cyclic loading conditions, regolith has been shown to continually deform with subsequent loadings, contrasting to quartz sands that exhaust all plastic deformations within the first cycle (Sandeep et al., 2019). Given that quartz sand is often modeled using simple discrete spheres, it stands to reason that a model well-suited for simulating regolith or any irregular, coarse grain could be improved by adopting a different grain geometry. A growing segment of literature has exemplified this. The study of railroad ballast - the coarse gravel piled beneath railroad ties - adopts polyhedral grains in discrete simulation (Lobo-Guerrero and Vallejo, 2006; McDowell and Li, 2016; Suhr and Six, 2017; Li and McDowell, 2018). Recent models of rubble-pile asteroids have adapted to simulate polyhedral grains instead of standard spherical grains (Ferrari et al., 2019; Ferrari and Tanga, 2020; Sánchez et al., 2021). Also, poly-ellipsoidal grains are shown to better replicate the experimental results of a rover wheel digging in regolith simulant compared to spherical grains (Knuth et al., 2012).

Driven by the trend towards modeling angular grains, the sparsity of relevant impact literature, and the potential wealth of knowledge in observing sub-surface granular dynamics, we use Finite Element Method (FEM) - via commercial software Abaqus - to discretely simulate a two-dimensional granular system impacted by a disk-like projectile. Since this is our first attempt at this FE-based discrete model, the media is composed of mono-disperse triangular grains which permit study of a non-conventional geometry without complexities that may make simulations unstable. Two-dimensional methods also follow the theme of simplicity and will streamline data extraction and calculation procedures for viewing sub-surface dynamics. These simulations offer access to bulk data for each element of the virtual system. This enables a deeper level of system analysis that is often unattainable with experimental methods. The packing of grains within a granular system show how they can re-arrange or position themselves in response to a dynamic event (Arévalo et al., 2010; Clark et al., 2012; Jia et al., 2012; Kondic et al., 2012; Xu et al., 2014; Zhao et al., 2017). Such packings are observable experimentally with X-ray tomography (Fu et al., 2006; Moreno-Atanasio et al., 2010; Weis and Schröter, 2017; Reimann et al., 2017), though simulations allow the same perspective but with reduced hassle. We will show this using an adapted form of Voronoi tessellation (Voronoi, 1908). Sub-surface strain distribution caused surface impacts are also studied, an approach seen in literature (Chen et al., 2011; Guo and Zhao, 2016; Luo et al., 2017).

The application of FEM for discrete simulations is present in the literature, albeit sparse. In the simulation of a two-dimensional shear cell, Kabir et al. (2008) used FEM to model discrete triangular, circular, and square grains with multiple elements per grain, visualizing force chains developed within the cell. Some angular DEM simulations have also used FEM as an intermediary between simulation steps to facilitate breakage of grains during modeling of rockfill (Bagherzadeh Kh. et al., 2011; Raisianzadeh et al., 2018, 2019; Seyyedani et al., 2021; Nitka and Tejchman, 2020). The field of multi-particle finite element method (MPFEM) simulates powders discretely with individual meshes to observe powder compaction under load (Güner et al., 2015; Zhang et al., 2015).

Section 2 will review the simulation design, procedures for conducting impact tests, and the ranges of impact conditions evaluated. Section 3 will review modeling results. Finally, Section 4 will summarize findings and re-iterate their broader implications. Appendix I showcases additional simulation work that verifies the performance of the Abaqus platform against LAMMPS DEM software. Appendix II publishes additional figures from the subsurface analysis of Section 3.2.

2. Simulation methods and setup

We use two-dimensional discrete triangles of equal size as the base grain geometry. This selection of a simple and monodisperse grain is intentional to improve model stability during development. The simplicity will also assist post-processing algorithms later on.

The simulation is comprised of a circular impactor and the grains. The impactor has diameter of 16.15mm and the edge length of the right-triangle grain is 3mm, giving a impactor-to-grain size ratio of 5.38. Both entities are modeled

Table 1
Material properties used in DEM simulation

	grain density (kg/m^3)	Young's modulus (GPA)	Poisson ratio
disk	2500	4.5	0.2
grains	2600	7.0	0.2

Table 2
Details of the gravity-based shake applied to further settle the granular bed. Negative accelerations are directed downwards.

sim time (s)	0	0.3	0.55	0.8	1.1	1.4
gravity (m/s^2)	-9.81	-9.81	+5.0	-12.0	-9.81	-9.81

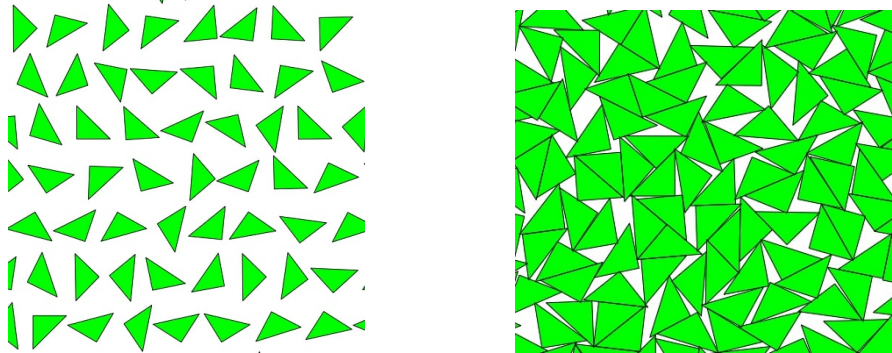


Figure 1: The granular bed is formed from an initial sparse patterning of randomly oriented and shifted grains (*left*) that are allowed to fall and settle under gravity (*right*)

as elastic bodies with the material properties shown in Table 1. In this work, the system is under Earth-like gravity to improve stability of the simulation and enable comparison to experimental literature for qualitative verification of model performance. The study of impacts in low gravity has been left for future reports.

To set up the system, a lattice is positioned above the rigid bin. A triangular grain is created and randomly positioned and oriented within each lattice cell. An external MATLAB code generates the vertex coordinates for all grains and writes those coordinates to a text file to be referenced by the Abaqus input file which will control the bed-settling stage of the simulation. The initial patterning of grains and their randomized orientation is shown in the left pane of Figure 1. Each grain was meshed as one single three-node linear plane strain element (CPE3 type). The impactor was discretized into thirty-two, four-node bilinear plane strain quadrilateral elements with reduced integration (CPE4R).

An automatically chosen, flexible time increment was used to execute the simulations. This selection is a feature of Abaqus where a stable time increment is computed as a factor of the shortest time for a dilatational wave to cross an element in the model.

To form the granular bed, the grains are allowed to fall freely and settle under Earth's gravity into the rigid bin. The interaction between all of the grains as well as the impactor are defined using a friction coefficient of $\mu = 0.85$, appropriate for coarse gravel (Wright et al., 2021). A ramped acceleration-based shake is applied to the settled granular bed to further settle the system. The details of the vertical shake procedure are included in Figure 2. Under the final gravity condition, the simulation is allowed to run until the total energy - calculated by Abaqus as the sum of strain energy, kinetic energy, viscous dissipation, frictional dissipation, and internal heat energy - stabilizes to a constant value.

The dimensions of the granular bed are approximately 0.32 m long and 0.16 m deep. The depth is intentionally about 10 times the diameter of the impactor. The length is such that, for a 30° impact at 10 m/s, the peak reaction force felt by the rigid container is approximately 5% of the peak reaction force felt by the projectile. This indicates the vast majority of energy is dissipated within the granular material and that effects of the rigid container on projectile response are minimal.

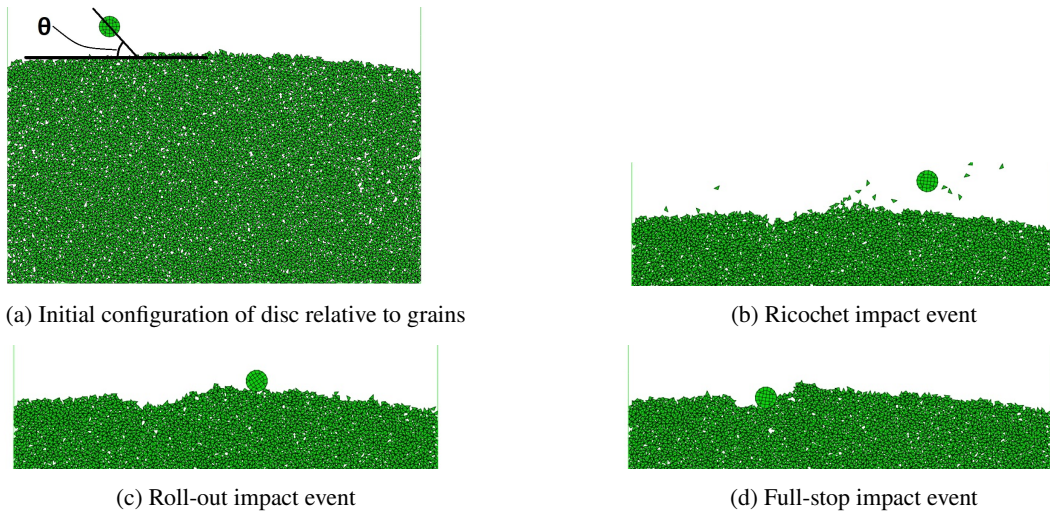


Figure 2: The initial configuration of impactor and granular bed system with impact angle convention (a) and final frame grabs of the three impact types (b-d). Panels (b) through (d) do not display the full depth of the granular bed for space-saving in print.

An impact is simulated by accelerating the projectile, shown in starting position about 2.2cm above the bed in Figure 2a, with a one millisecond impulse to achieve desired impact velocity and approach angle. The impactor is also subjected to Earth-like gravity. It is assumed that the impact angle and velocity is minimally impacted by gravity acting on the projectile; for the lowest velocity and shallowest impacts, which are most affected, gravity was observed to change impact angle by only a couple of degrees and velocity by a small fraction of a meter-per-second.

An example snap-shot of each impact behavior type is shown in Figure 2. A ricochet event occurs when the impactor departs the initial crater, breaking contact with the granular bed (see Figure 2b). The roll-out event occurs when the impactor rolls out of the initial impact crater but does not break contact with the granular surface (see Figure 2c). The full-stop impact behavior occurs when the impactor comes to a complete stop in the initial impact crater (see Figure 2d).

We carry out two batches of impact simulations. Section 3.1 reviews the macro behavior of two-hundred eighty six impact simulations with velocities ranging from 1 m/s to 7 m/s and angles between 20° and 70° (measured from horizontal). These ranges are selected based on literature to ensure a full span of impactor behaviors. Section 3.2 studies eighteen simulations; nine at an impact angle of 30° ranging from 2 m/s to 10 m/s and nine at 60° over the same velocity range. To present this work on the same plane as Wright et al. (2020), we also report the dimensionless Froude number of each impact, calculated in terms of projectile velocity v , radius r , and gravitational acceleration g by the expression v/\sqrt{gr} .

3. Results & Discussions

3.1. Impact behavior mapping

In this section, we carry out analysis of the simulations in order to understand how impactor behavior evolves with impact angle and velocity. Denoting each set of initial conditions and their corresponding post-impact behavior as a distinct marker, Figure 3a shows the impact behavior map obtained from the setup in Figure 2a. Red squares represent ricochet impact events (ric), blue diamonds represent roll-out events (ro), and black circles represent full-stop events (fs). Red diamonds represent a hybrid ricochet/roll-out event (ro/ric), where impactor may have become partially airborne after contact as it moves away from the impact crater. Blue squares represent a hybrid full-stop/roll-out event (fs/ro), where the impact clearly does not settle in the basin of the initial crater but does not completely escape it either.

Inspection of Figure 3a reveals several features of interest. In the lower right region at higher velocities and lower impact angles, the ricochet impact response dominates. In the upper left region at lower velocities and steeper impact angles, a full-stop behavior dominates. Full-stop behavior also appears in a band across the top of the figure, for the steepest impact angle of 70° . In-between the full-stop zones and ricochet zones, the roll-out events appear as a

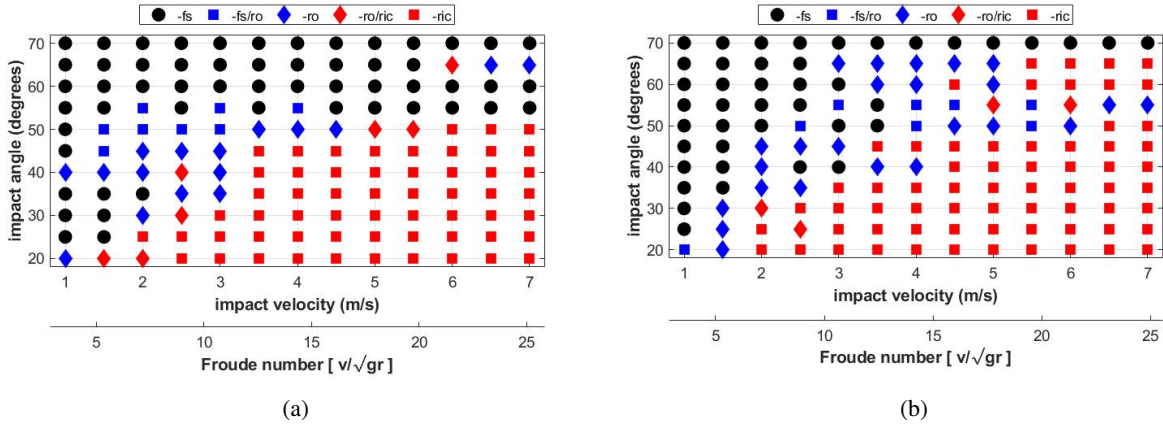


Figure 3: Impact event classification as a function of impact angle and impact velocity for (a) the initial configuration from Figure 2a and (b) the same system with the impact site shifted by 5mm.

Table 3

Results of simulations at different bed depths.

impact angle	impact velocity	original bed result	deep bed result
30°	10 m/s	ricochet	ricochet
60°	10 m/s	full-stop	ricochet
70°	10 m/s	ricochet	full-stop

transitional behavior. These regions and their relative positions are consistent with experimental findings by Wright et al. (2020), though it is noted that quantitative agreement is neither expected nor observed due to numerous differences in system specifications such as grain-to-projectile size ratio and the triangular grain geometry. Experimental work is also three dimensional whereas simulations are constrained to two dimensions, which may greatly impact comparisons.

In Figure 3a, an out-of-place cluster of impact events is observed for 65° impacts between 6 m/s and 7 m/s. In this position, where full-stop behavior would be expected, roll-out and ricochet behavior is recorded instead. To test whether this oddity persists, simulations are repeated with the impactor positioned 5 mm to the right. The 5 mm adjustment represents a shift of close to two grain lengths, ensuring that the impactor will be hitting different regions of the surface. The impact behavior map produced under the shifted configuration is shown in Figure 3b. It is found that the same pocket of impacts at 65° now presents ricochet behavior whereas ricochet (lower right) and full-stop (upper left) regions remain largely unchanged.

This finding is intriguing. What mechanism could cause this type of behavior change? Can a small shift in the location of the impact really influence the resulting behavior so significantly? To solidify the finding, we rule out granular bed depth as the causal factor. If the granular bed is too shallow, a stochastic effect caused by the rigid bin wall could undermine repeatability and affect impact behavior. Six additional simulations at 10 m/s and 30°/60°/70° impact angles are run on the original granular bed and on a newly generated bed that is approximately 1.5 times the depth of that shown in Figure 2a. 10 m/s represents the highest velocity tested in this work and thus the highest energy impact we test, so an assessment of adequate bed depth in this condition would carry through to all simulations presented. The results of the six simulations are presented in Table 3.

No behavior change is observed for the 30° simulations, suggesting bed depth is not an influential factor and that the original bed is sufficient. Results for 60° and 70° impacts are more ambiguous, showing behavior change from full-stop to ricochet for 60° and from ricochet to full-stop for 70°. If bed depth is a factor here, it is inconsistent in how it affects the impact behaviors as the 70° impact shows the opposite behavior change from the 60° impact. Instead, the behavior change we see is more aligned with observations from Figure 3, where bed depth was not changed between panels (a) and (b). In the upper right regions, behavior changes from full-stop to ricochet and vice-versa are not just observed, but widespread. From this, we suggest that the behavior changes are attributed to the change in impact

location and not due to stochasticity from the lower rigid boundary; the depth of the original bed is sufficient for this work.

The mechanism that causes impact behaviors to be sensitive to impact location remains unknown. Perhaps surface topography alone could be the culprit, since the grain size used in this work is quite large relative to the impactor. This explanation would agree with theories from Wright et al. (2021), where it was suggested that as grain size relative to the projectile decreases, the response of the projectile stabilizes and becomes less dependent upon surface topography. Of course, the invisible force chain network that absorbs the impactor energy may also play a role and that impacting at a different location may change how it is able to respond. But for either of these explanations, why do the plots of Figure 3 suggest that this location-sensitivity is only observed under certain impact conditions? These questions are undoubtedly complex and will warrant a dedicated study in future work.

3.2. Sub-surface quantification

3.2.1. Packing fraction analysis

In this section, post-processing of simulation data from impacts angled at 30° and 60° reveal information about the sub-surface granular dynamics that occur during a surface impact. This is a meaningful study because such dynamics contribute to the behavior of the impactor due to the dissipation of energy through grains. Such pathways of dissipation are affected by how grains are positioned relative to their neighbors and the incoming impulse from the impactor. For instance, loose packing of grains could lead to compactification and slippage between grains and a gradual dissipation of energy by friction, creating an overall cushioning effect on an impactor. Tighter grain packings may lead to direct transmission of forces along force chains, producing a stouter impactor behavior reminiscent of solid-on-solid impact.

Impactor behaviors and sub-surface granular mechanics can be tied together by considering changes in grain packing density and its distribution. Typically packing analysis is done by evaluating a system's overall change in packing density, though discrete simulation method can provide a better understanding of such change by considering its spatial distribution.

The void mapping procedure stems originally from Point Voronoi tessellation (Voronoi, 1908), a method that can take a random collection of points and divide the surrounding space into convex polygonal regions belonging to each point. Point Voronoi tessellation may also be used for collections of uniform circles (An et al., 2021) or lightly adapted with weighting techniques for poly-disperse circles (Morley and Wilson, 2020).

However, Point Voronoi tessellation is insufficient for mapping void space between more complex geometries because centroids of particles are no longer equidistant from the edges. Therefore, tessellated regions may cut off parts of the parent grain, causing inaccuracies in packing fraction calculation. This limitation inspired the Set Voronoi tessellation method (Schaller et al., 2013; Dong et al., 2016; Zhang et al., 2021), an evolution of the Point Voronoi procedure for irregular geometries that uses additional discretization and unification steps. In this work, MATLAB's built-in Point Voronoi function has been merged with the additional steps of Set Voronoi tessellation to permit accurate division of void space among the triangular grains. The details of the process are described below:

1. Raw positional data is read in and rearranged into a more accessible format.
2. Each grain is shrunk to improve the accuracy of the Voronoi tessellation procedure. Relative to the centroid of each grain, vertex coordinates are adjusted to reduce the size of the grain by a certain factor.
3. The edges of grains are discretized. Based on a certain length increment, additional points created between the vertices and added to the overall point-set for each grain.
4. A set of points bounding the full granular bed is generated to constrain the Voronoi tessellation and maintain accuracy at the edges of the granular bed.
5. Combining the data points belonging to the grains with the points belonging to the boundary, the whole structure is passed to the MATLAB's built-in 'voronoi' function which completes the first step of the tessellation.
6. Resulting polygonal cells created for each point are united together according to their parent grains. The merger of these polygons produces the final 'spatial cell' of the granular bed that a particular grain owns.
7. Finally, a local packing fraction (ϕ_{local}) is estimated for each grain by dividing the area of the grain itself (A_{grain}) by the area of its spatial cell (A_{cell}) such that $\phi_{local} = A_{grain}/A_{cell}$.

Figure 4a depicts a few grains positioned based on data exported from simulations. Figure 4b depicts these grains after they are shrunk and discretized with additional points along its boundary. Figure 4c shows the result of MATLAB's Voronoi tessellation utility which divides up the space in-between points to spatial allotment closest to

Subsurface dynamics in oblique granular impacts

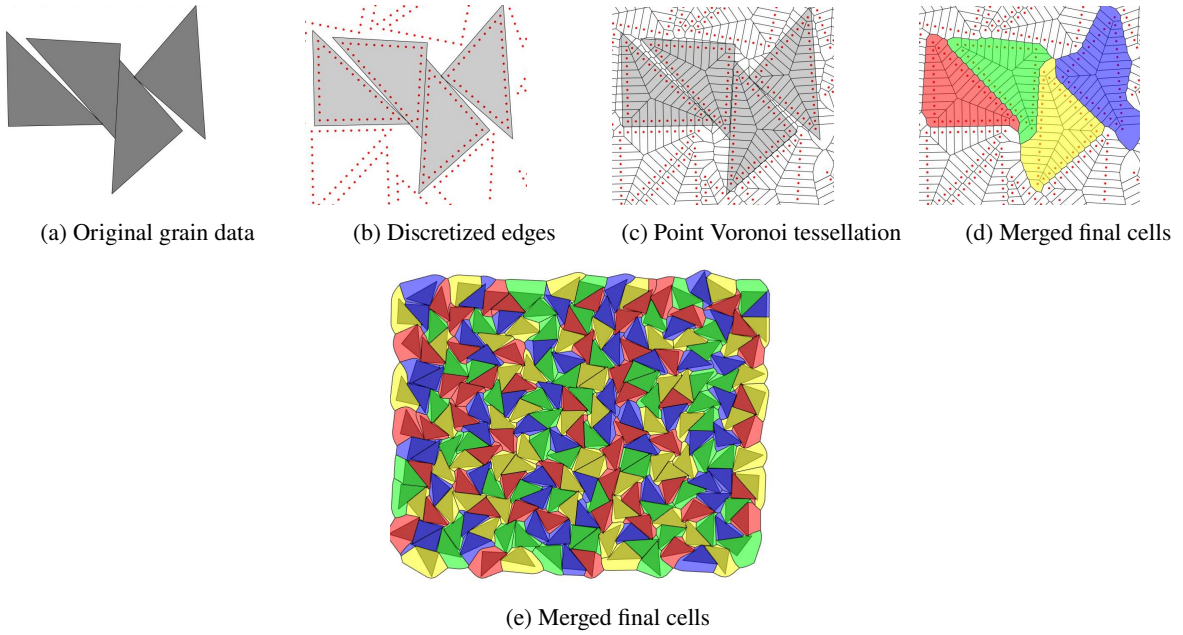


Figure 4: The tessellation procedure for calculation of grain-level packing fraction.

a particular point. Figure 4d illustrates how the post-processing script merges the polygons belonging to the larger grain into one larger polygon. Figure 4e shows the final result of the tessellation procedure, with a polygonal cell that represents the region of the granular bed belonging to a grain. The original grain is overlaid in Figure 4e to show the two regions which are used for computing packing fraction. Each color in Figure 4e corresponds to the core that calculated that Voronoi cell, as parallel processing was used to expedite post-processing.

The procedure outlined allows for calculation of grain-level packing fraction and such a result is shown in Figure 5a, depicting a homogeneous distribution of overall packing density in the granular bed before an impact. This indicates that the bed is as compact as possible and that porosity was consistent across all our simulations.

A histogram of packing fraction measurements from Figure 5a is shown in the black bars of Figure 5b. A neat bell curve is produced, indicating a well-settled granular bed.

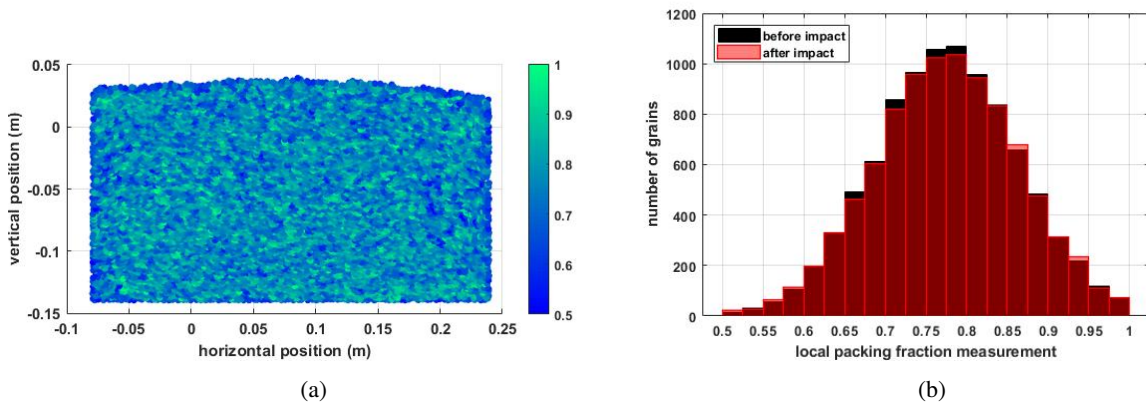


Figure 5: Evaluation of pre-impact granular bed quality using local packing fraction estimates. A colored packing density plot shows the raw local packing fraction measurements (a), and a histogram (b) illustrates the distribution of these packing fraction measurements.

Originally, to demonstrate the reconfiguration, plain packing fraction measurements after impact were assessed in the same manner shown in Figure 5a. In Figure 5b, the after-impact histogram for a 10 m/s, 30° scenario is overlaid on the pre-impact data with the red bars. Unfortunately, the shift is slight and uninformative from this perspective. The poor visualization also suggests that holistic packing fraction for the entire bed, as would be typically measured with fluid displacement or bulk density, would also fail to capture any grain restructuring.

Instead, the per-grain change in packing fraction was found to be a better metric. Figure 6 presents packing density plots of each velocity case for 60° impacts. Results for 30° simulations may be found in Appendix II. For each grain, the packing fraction post-impact is subtracted from its pre-impact value, so a positive change in packing fraction indicates grain patterns tightening whereas a negative change implies loosening.

The upper and lower limits of the colorbar indicate a positive or negative change in packing fraction of approximately 8.7%, which is taken from the standard deviation of pre-impact packing fraction measurements in Figure 5b. The plots of Figure 6 show how the breadth of disturbance changes with higher velocity impacts.

Considering the 2 m/s density plot (Figure 6a), it is shown that only grains immediately around the impact crater reconfigure asymmetrically, within about a one to two impactor diameter radius. Disturbance is contained to this zone, and surrounding surface and sub-surface grains remain relatively undisturbed.

Figure 6e shows that for an impact at 6 m/s the density plot has a region of disturbed grains that has clearly grown with a tripling of the impactor velocity. Interestingly, the right side of the crater shows a zone of grains in which porosity has increased compared to other regions around the crater where grains have packed closer together. Velocities equal to or greater than 6 m/s also show ejecta that has been strewn along the surface, evident from the trail of overall shifted grains extending along the surface beyond the crater.

Finally, at 10 m/s (Figure 6i), all aspects of the granular disturbance are amplified. The region of disturbed grains around the crater is roughly about four to five times the diameter of the impactor, the scattered ejecta layer along the surface is much more prominent and several grains deep, and there are even pockets of shifted grains deeper within the granular bed outside of the primary disturbed zone. This latter observation is attributed to structural instabilities within the granular bed that hold up for lower velocities but begin to collapse for higher velocities and indicates that a pressure pulse has propagated through the medium.

These findings intuitively demonstrate how the region of disturbed grains increases steadily with impactor velocity. This trend is shown in both 60° and 30° impact results. However, these two groups of findings differ when considering the asymmetry of the sub-surface disturbance. For instance, comparing the 10m/s packing fraction density plots for 30° (Figure 13i) and 60° (Figure 6i), the former produces a much more asymmetrical compacted zone around the crater and the spread of ejecta across the surface still leaves some area uncovered. This observation does not hold for the 60° case where virtually the entire surface of the granular bed has been covered with ejecta and the grain disturbance beneath the surface is slightly more symmetrical.

3.2.2. Strain distributions

Reconfiguration of grains are not necessarily accompanied by a change in packing fraction, so other perspectives should be sought out. Therefore, we compute the strain on each grain using displacement fields. A large-strain Eulerian formulation, shown in Equation 1 in summation index notation, shows how we calculate the strain tensor from the displacement fields of the grains u .

$$\epsilon_{ij} = \frac{1}{2} \left(\frac{\partial u_i}{\partial x_j} + \frac{\partial u_j}{\partial x_i} \right) - \frac{1}{2} \frac{\partial u_m}{\partial x_i} \frac{\partial u_m}{\partial x_j} \quad (1)$$

Here, it is implied that we sum over index m .

To collapse the strain tensor for each grain to a single representative value, the von Mises distortion is calculated as follows

$$\epsilon_{\text{von Mises}} = \sqrt{\frac{2}{3}} (\epsilon' : \epsilon'). \quad (2)$$

where ϵ' represents the deviatoric strain tensor, with components given by $\epsilon'_{ij} = \epsilon_{ij} - \frac{1}{3} \delta_{ij} \epsilon_{kk}$ and δ_{ij} represents Kronecker delta function. The $:$ symbol represents a sum over both indices, $\epsilon' : \epsilon' = \sum_{ij} \epsilon'_{ij} \epsilon'_{ij}$.

Subsurface dynamics in oblique granular impacts

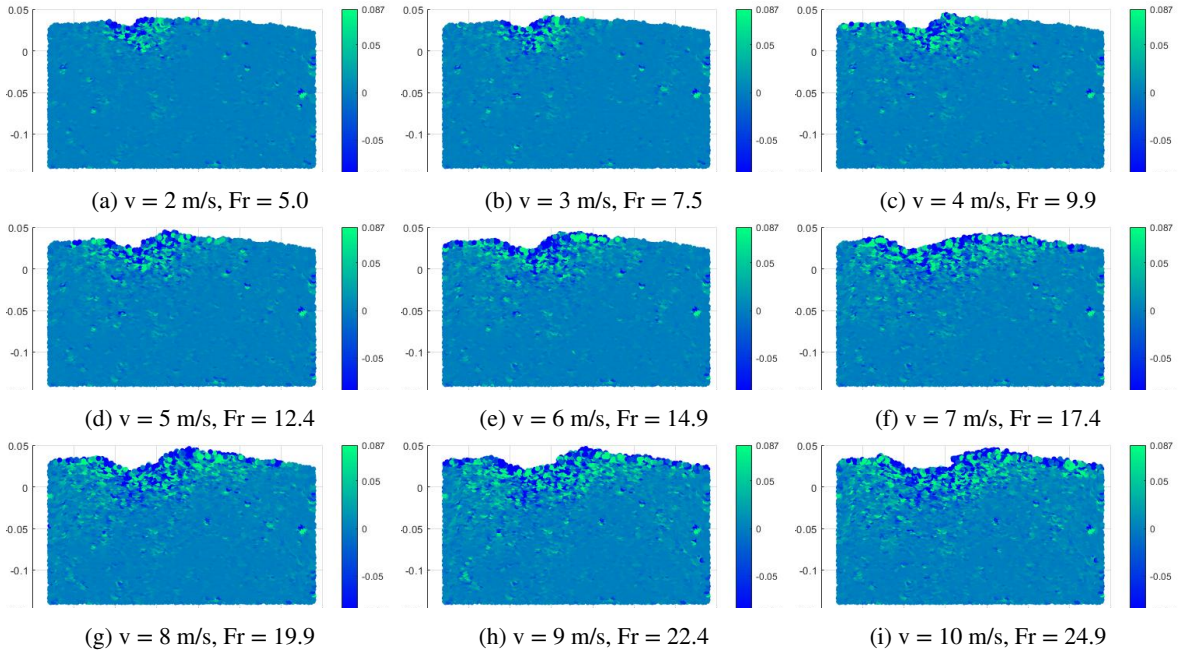


Figure 6: Colored packing density plots illustrating the local packing fraction changes after impacts of various velocities at 60° from the horizontal. Velocity and Froude number of each impact are reported.

To visualize the strained region around the impact crater, the contour plot is set to only two levels of contour, the threshold of which is set at a strain level for the von Mises distortion $\epsilon_{\text{von Mises}} = 3 \times 10^{-4}$. This value is based on a quasi-static flow strain measurement calculated from separate simulation. Using the same granular bed, a 5 cm horizontal rigid plate is positioned just above the surface. A displacement boundary condition pushes the plate downward at a rate of 0.25 mm/s for 1 cm, breaking through the granular surface. Reading the reaction force against the plate reveals the time at which the surface yields and then post-processing the grain displacement data at that frame gives the local strain corresponding to the yield, found to be 3×10^{-4} .

Figure 7 displays the strain contours for the 60° impact cases. Figure 14, in Appendix II, shows results for 30° .

Figure 7a shows the distortion contour plot for the lowest velocity 2 m/s impact. As was shown with the relative packing fraction results, the strained region of grains is largely confined to the impact crater. A moderate velocity level of 6 m/s in Figure 7e demonstrates a larger region of strained grains with a noticeable strained layer to the right of the impact crater, indicating ejecta along the surface. In Figure 7i at 10 m/s, all features of the 6 m/s case are further amplified except, seemingly, for the depth of the perturbed region. Otherwise, the layer of surface-scattered material is much deeper as is the span of the directly strained region around the impact site. Figure 7 also illustrates the asymmetry in substrate response caused by the oblique impact mentioned in the packing fraction analysis.

The observation that depth of the strained region did not continue to grow for higher velocity impacts at 60° spurred further study of the strain contours. On each plot of Figure 7 and Figure 14, two red lines are traced. The upper red line indicates the surface of the deformed granular bed, generated automatically in post-processing from grain positional data. The lower red line follows the bottom of the disturbed region. The two red lines meet at each end, enclosing a region denoted the 'skin zone'. The skin zone, therefore, represents the region of grains that have been plastically strained beneath the surface as well as the layer of ejected grains that have settled atop the surface. The difference in height between corresponding points of upper and lower boundaries produces a 'skin depth' measurement.

Figure 8 shows skin depth measurements versus horizontal position for 30° and 60° impacts. For easier viewing, the results are smoothed with a moving average and a vertical shift to align the leftmost points. The smoothing helps to view the trend in skin zone geometry with increasing velocity impacts.

In Figure 8a, showing 30° impacts, a fairly straightforward trend is seen where the skin zone deepens and widens in a steady manner as velocity increases. Contrast to this the 60° impacts in Figure 8b. Starting from the blue line, representing the 2 m/s case, a single sharp peak is shown with a general return to zero moving further to the right. The

Subsurface dynamics in oblique granular impacts

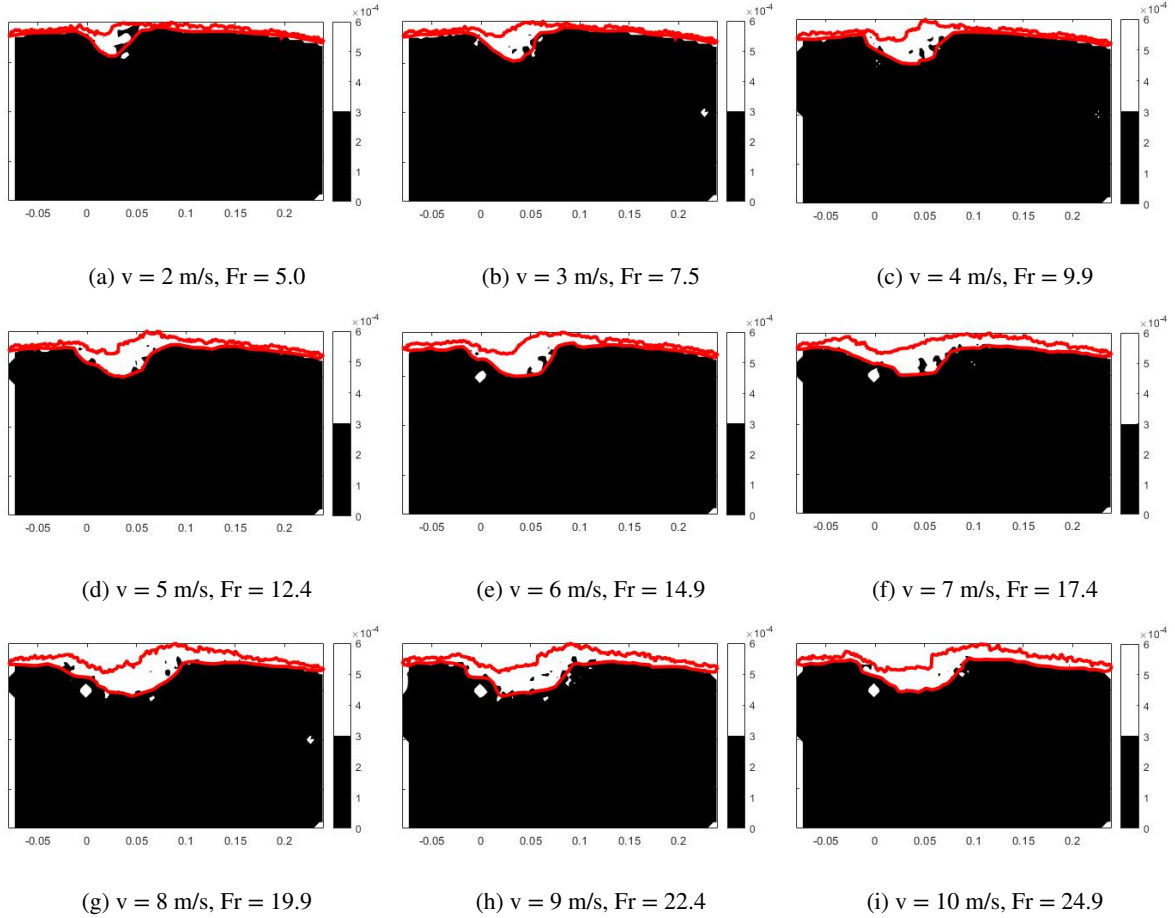


Figure 7: Contour plots of Von Mises strain distribution in the granular bed after impacts of various velocities at 60° from the horizontal. Velocity and Froude number of each impact are reported.

next five impact cases, up to about 6 m/s, show that same sharp peak continue to grow accompanied by a levelling out of the zone moving to the right. However, for 7 m/s impacts and above, the peak no longer grows and instead reduces in height and widens out as lateral strain appears to dominate over strains deeper in the bed.

The observed trend of peaks in the skin zone depth measurements for 60° suggests a potential change in the response of the granular media to the surface impacts of increasing velocity. Up until a point, the strained region does grow deeper with increasing velocity. However, around 7 m/s for this specific scenario, the peak shortens with deeper plastically deformed regions spanning further to the left and right of the impact crater. We have not been able to identify this type of trend in literature though it suggests that the energy dissipation mechanism that arrests projectile motion may change with increasing velocity, leading to a more lateral plastic deformation.

To further investigate this trend's dependence on velocity, the raw skin depth measurements are averaged to create a data point for mean skin depth at corresponding impact velocity. The data are displayed in Figure 9, where mean skin depth (MSD) measurements for 30° impacts and 60° impacts are marked by red squares and blue circles, respectively. Additionally, for each simulation, measurements of the transient crater depth (TCD) - the deepest point to exist in the crater during the impact event - are also displayed for 30° and 60° impacts as red and blue dashed lines.

From the four data sets of Figure 9, some interesting discussions arise. The MSD data from both 30° and 60° simulations closely overlap each other until around 9 m/s. The similarities in these MSD data persist despite predominantly ricochet behavior in the 30° impact simulations and full-stop behavior in the 60° cases and drastically different components of vertical and horizontal components of velocity upon impact. For instance, at the 5m/s case, the mean skin depth of the 30° impact is near identical to 60° . The TCD data, on the other hand, show that crater depths

Subsurface dynamics in oblique granular impacts

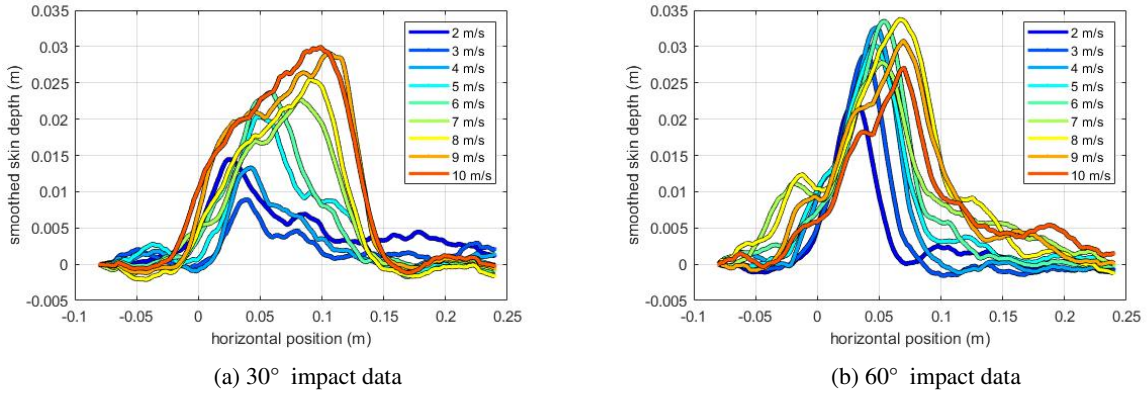


Figure 8: Plots of skin depth - the difference in height between corresponding points on the upper and lower boundaries shown in versus horizontal position.

are generally greater for across the velocity range for 60° impacts than for 30° impacts. Furthermore, the TCD data for 60° also closely aligns with the MSD data for 60° . This last observation suggests that for such an angle in these specific conditions, measuring crater depth at the surface directly reveals the mean depth of the disturbed grain region beneath.

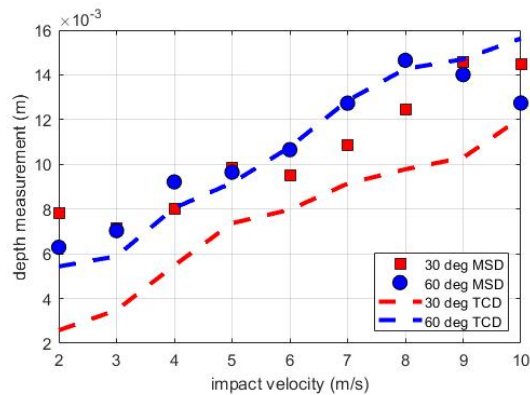


Figure 9: Plots of Mean Skin Depth (MSD) and measured Transient Crater Depth (TCD) for 30° (red) and 60° (blue) impacts.

4. Conclusion

Simulation work has been used to study new facets of low-velocity oblique impacts into a granular media. Citing trends in granular dynamics literature toward modeling angular grain geometries as a better representation of ET regolith, this work has developed discrete 2D simulations, based in finite elements, that model the simplest possible polygonal grain geometry – the triangle. Maintaining Earth-like gravity to improve simulation stability and enable comparison to experimental literature, impacts at various angles and velocities of a circular projectile into a bed of triangular grains have been simulated.

Our simulations demonstrate the three classes of impact behavior and reproduce the velocity and impact angle dependent division between ricochet and roll-out behaviour, recently observed in experiments (Wright et al., 2020).

We find that visualizing the per-grain local packing fraction variance within 8.7% reveals a sub-surface perturbed region that is lopsided with respect to the impact point. Local porosity variations are focused in front of the impact site by a distance that is similar in size to the crater radius. The region in front of the impact can be compacted while substrate nearer the surface increases in porosity. Strain analyses introduce the notion of 'skin zone', or the

region beneath the surface that is strained beyond the quasi-static yield threshold. Measurements of this skin zone have demonstrated trends that suggest granular dissipative mechanisms change when faced with increasing impact velocity.

There is more work to do. Mono-disperse triangular grains are not reflective of any naturally occurring material and their use here was to ease development of the FE-based model. Because the approach was successful, further iterations will model more complex polyhedral grain geometries in three dimensions. Various gravity conditions, extending to micro-gravity, will be studied. Polydispersity, another key characteristic of regolith, will also need to be considered to bring simulations closer in line with reality. Implementation of these next considerations will be facilitated by the script-automated model generation we have used here.

Developing a comprehensive understanding of the phenomena entailed in asteroid impacts would support space missions targeting asteroid and planetary exploration. Successful research in this field would have ripple effects into other research. Improved simulations of regolith media and deeper understanding of its behavior in response to stimuli could aid development of surface vehicles and drilling equipment or aid the study of in situ building materials.

Acknowledgements

This material is based on work partially supported by NASA grant 80NSSC21K0143

References

- An, X., Dong, K., Yang, R., Zou, R., Yu, A., 2021. On the relationships between structural properties and packing density of uniform spheres. *Powder Technology* 388, 139–148. URL: <https://www.sciencedirect.com/science/article/pii/S0032591021003661>, doi: <https://doi.org/10.1016/j.powtec.2021.04.079>.
- Arévalo, R., Zuriguel, I., Maza, D., 2010. Topology of the force network in the jamming transition of an isotropically compressed granular packing. *Phys. Rev. E* 81, 041302. URL: <https://link.aps.org/doi/10.1103/PhysRevE.81.041302>, doi: [10.1103/PhysRevE.81.041302](https://doi.org/10.1103/PhysRevE.81.041302).
- Bagatin, A., Petit, J.M., Farinella, P., 2001. How many rubble piles are in the asteroid belt? *Icarus* 149, 198–209. URL: <https://www.sciencedirect.com/science/article/pii/S001910350096531X>, doi: <https://doi.org/10.1006/icar.2000.6531>.
- Bagherzadeh Kh., A., Mirghasemi, A., Mohammadi, S., 2011. Numerical simulation of particle breakage of angular particles using combined dem and fem. *Powder Technology* 205, 15–29. URL: <https://www.sciencedirect.com/science/article/pii/S0032591010003815>, doi: <https://doi.org/10.1016/j.powtec.2010.07.034>.
- Brisset, J., Colwell, J., Dove, A., Abukhalil, S., Cox, C., Mohammed, N., 2018. Regolith behavior under asteroid-level gravity conditions: low-velocity impact experiments. *Progress in Earth and Planetary Science* 5, 73. URL: <https://doi.org/10.1186/s40645-018-0222-5>, doi: [10.1186/s40645-018-0222-5](https://doi.org/10.1186/s40645-018-0222-5).
- Burns, J.A., 1975. The angular momenta of solar system bodies: Implications for asteroid strengths. *Icarus* 25, 545–554. URL: <https://www.sciencedirect.com/science/article/pii/0019103575900354>, doi: [https://doi.org/10.1016/0019-1035\(75\)90035-4](https://doi.org/10.1016/0019-1035(75)90035-4).
- Chen, Q., Andrade, J.E., Samaniego, E., 2011. Aes for multiscale localization modeling in granular media. *Computer Methods in Applied Mechanics and Engineering* 200, 2473–2482. URL: <https://www.sciencedirect.com/science/article/pii/S0045782511001630>, doi: <https://doi.org/10.1016/j.cma.2011.04.022>.
- Clark, A.H., Kondic, L., Behringer, R.P., 2012. Particle scale dynamics in granular impact. *Physical review letters* 109, 238302–238302.
- Cundall, P.A., Strack, O.D.L., 1979. A discrete numerical model for granular assemblies. *Géotechnique* 29, 47–65. URL: <https://doi.org/10.1680/geot.1979.29.1.47>, doi: [10.1680/geot.1979.29.1.47](https://doi.org/10.1680/geot.1979.29.1.47), arXiv: <https://doi.org/10.1680/geot.1979.29.1.47>.
- Dong, K., Wang, C., Yu, A., 2016. Voronoi analysis of the packings of non-spherical particles. *Chemical Engineering Science* 153, 330–343. URL: <https://www.sciencedirect.com/science/article/pii/S0009250916303785>, doi: <https://doi.org/10.1016/j.ces.2016.07.013>.
- Dowling, D.R., Dowling, T.R., 2013. Scaling of impact craters in unconsolidated granular materials. *American journal of physics* 81, 875–878.
- Ferrari, F., Lavagna, M., Blazquez, E., 2019. A parallel-GPU code for asteroid aggregation problems with angular particles. *Monthly Notices of the Royal Astronomical Society* 492, 749–761. URL: <https://doi.org/10.1093/mnras/stz3458>, doi: [10.1093/mnras/stz3458](https://doi.org/10.1093/mnras/stz3458), arXiv: <https://academic.oup.com/mnras/article-pdf/492/1/749/31731024/stz3458.pdf>.
- Ferrari, F., Tanga, P., 2020. The role of fragment shapes in the simulations of asteroids as gravitational aggregates. *Icarus* 350, 113871. URL: <https://www.sciencedirect.com/science/article/pii/S0019103520302517>, doi: <https://doi.org/10.1016/j.icarus.2020.113871>.
- Fu, X., Dutt, M., Benthall, A.C., Hancock, B.C., Cameron, R.E., Elliott, J.A., 2006. Investigation of particle packing in model pharmaceutical powders using x-ray microtomography and discrete element method. *Powder Technology* 167, 134–140. URL: <https://www.sciencedirect.com/science/article/pii/S0032591006002348>, doi: <https://doi.org/10.1016/j.powtec.2006.06.011>.
- Goldman, D.I., Umbanhowar, P., 2008. Scaling and dynamics of sphere and disk impact into granular media. *Physical review. E, Statistical, nonlinear, and soft matter physics* 77, 021308–021308.
- Gou, S., Yue, Z., Di, K., Liu, Z., 2018. A global catalogue of ceres impact craters greater than 1 km and preliminary analysis. *Icarus* 302, 296–307. URL: <https://www.sciencedirect.com/science/article/pii/S0019103517303585>, doi: <https://doi.org/10.1016/j.icarus.2017.11.028>.

- Guo, N., Zhao, J., 2016. 3d multiscale modeling of strain localization in granular media. *Computers and Geotechnics* 80, 360–372. URL: <https://www.sciencedirect.com/science/article/pii/S0266352X16300027>, doi:<https://doi.org/10.1016/j.compgeo.2016.01.020>.
- Güner, F., Ömer Necati Cora, Sofuoğlu, H., 2015. Numerical modeling of cold powder compaction using multi particle and continuum media approaches. *Powder Technology* 271, 238–247. URL: <https://www.sciencedirect.com/science/article/pii/S0032591014009061>, doi:<https://doi.org/10.1016/j.powtec.2014.11.008>.
- Jia, T., Zhang, Y., Chen, J., 2012. Simulation of granular packing of particles with different size distributions. *Computational Materials Science* 51, 172–180. URL: <https://www.sciencedirect.com/science/article/pii/S0927025611004368>, doi:<https://doi.org/10.1016/j.commatsci.2011.07.044>.
- Kabir, M.A., Lovell, M.R., Higgs, C.F., 2008. Utilizing the explicit finite element method for studying granular flows. *Tribology Letters* 29, 85–94. URL: <https://doi.org/10.1007/s11249-007-9285-y>, doi:10.1007/s11249-007-9285-y.
- Knuth, M., Johnson, J., Hopkins, M., Sullivan, R., Moore, J., 2012. Discrete element modeling of a mars exploration rover wheel in granular material. *Journal of Terramechanics* 49, 27–36. URL: <https://www.sciencedirect.com/science/article/pii/S0022489811000619>, doi:<https://doi.org/10.1016/j.jterra.2011.09.003>.
- Kondic, L., Fang, X., Losert, W., O'Hern, C.S., Behringer, R.P., 2012. Microstructure evolution during impact on granular matter. *Physical review E, Statistical, nonlinear, and soft matter physics* 85, 011305–011305.
- Leinhardt, Z.M., Richardson, D.C., Quinn, T., 2000. Direct n-body simulations of rubble pile collisions. *Icarus* 146, 133–151. URL: <https://www.sciencedirect.com/science/article/pii/S001910350096370X>, doi:<https://doi.org/10.1006/icar.2000.6370>.
- Li, H., McDowell, G.R., 2018. Discrete element modelling of under sleeper pads using a box test. *Granular Matter* 20, 26. URL: <https://doi.org/10.1007/s10035-018-0795-0>, doi:10.1007/s10035-018-0795-0.
- Lobo-Guerrero, S., Vallejo, L.E., 2006. Discrete element method analysis of railtrack ballast degradation during cyclic loading. *Granular Matter* 8, 195. URL: <https://doi.org/10.1007/s10035-006-0006-2>, doi:10.1007/s10035-006-0006-2.
- Luo, T., Ooi, E., Chan, A., Fu, S., 2017. The combined scaled boundary finite-discrete element method: Grain breakage modelling in cohesionless granular media. *Computers and Geotechnics* 88, 199–221. URL: <https://www.sciencedirect.com/science/article/pii/S0266352X17300824>, doi:<https://doi.org/10.1016/j.compgeo.2017.03.012>.
- McDowell, G.R., Li, H., 2016. Discrete element modelling of scaled railway ballast under triaxial conditions. *Granular Matter* 18, 66. URL: <https://doi.org/10.1007/s10035-016-0663-8>, doi:10.1007/s10035-016-0663-8.
- Michel, P., Ballouz, R.L., Barnouin, O.S., Jutzi, M., Walsh, K.J., May, B.H., Manzoni, C., Richardson, D.C., Schwartz, S.R., Sugita, S., Watanabe, S., Miyamoto, H., Hirabayashi, M., Bottke, W.F., Connolly, H.C., Yoshikawa, M., Lauretta, D.S., 2020. Collisional formation of top-shaped asteroids and implications for the origins of ryugu and bennu. *Nature Communications* 11, 2655. URL: <https://doi.org/10.1038/s41467-020-16433-z>, doi:10.1038/s41467-020-16433-z.
- Michel, P., Tanga, P., Benz, W., Richardson, D.C., 2002. Formation of asteroid families by catastrophic disruption: Simulations with fragmentation and gravitational reaccumulation. *Icarus* 160, 10–23. URL: <https://www.sciencedirect.com/science/article/pii/S0019103502969484>, doi:<https://doi.org/10.1006/icar.2002.6948>.
- Moreno-Atanasio, R., Williams, R.A., Jia, X., 2010. Combining x-ray microtomography with computer simulation for analysis of granular and porous materials. *Particuology* 8, 81–99. URL: <https://www.sciencedirect.com/science/article/pii/S1674200110000210>, doi:<https://doi.org/10.1016/j.partic.2010.01.001>.
- Morley, D.O., Wilson, M., 2020. Voronoi diagrams in quasi-2d hard sphere systems. *Journal of Statistical Mechanics: Theory and Experiment* 2020, 093201. URL: <https://doi.org/10.1088/1742-5468/aba7af>, doi:10.1088/1742-5468/aba7af.
- Nakamura, T., Noguchi, T., Tanaka, M., Zolensky, M.E., Kimura, M., Tsuchiyama, A., Nakato, A., Ogami, T., Ishida, H., Uesugi, M., Yada, T., Shirai, K., Fujimura, A., Okazaki, R., Sandford, S.A., Ishibashi, Y., Abe, M., Okada, T., Ueno, M., Mukai, T., Yoshikawa, M., Kawaguchi, J., 2011. Itokawa dust particles: A direct link between s-type asteroids and ordinary chondrites. *Science* 333, 1113–1116. URL: <https://www.science.org/doi/abs/10.1126/science.1207758>, doi:10.1126/science.1207758, arXiv:<https://www.science.org/doi/pdf/10.1126/science.1207758>.
- Nitka, M., Tejchman, J., 2020. Comparative dem calculations of fracture process in concrete considering real angular and artificial spherical aggregates. *Engineering Fracture Mechanics* 239, 107309. URL: <https://www.sciencedirect.com/science/article/pii/S0013794420308912>, doi:<https://doi.org/10.1016/j.engfracmech.2020.107309>.
- Noguchi, R., Hirata, N., Hirata, N., Shimaki, Y., Nishikawa, N., Tanaka, S., Sugiyama, T., Morota, T., Sugita, S., Cho, Y., Honda, R., Kameda, S., Tatsumi, E., Yoshioka, K., Sawada, H., Yokota, Y., Sakatani, N., Hayakawa, M., Matsuoka, M., Yamada, M., Kouyama, T., Suzuki, H., Honda, C., Ogawa, K., Kanamaru, M., ichiro Watanabe, S., 2021. Crater depth-to-diameter ratios on asteroid 162173 ryugu. *Icarus* 354, 114016. URL: <https://www.sciencedirect.com/science/article/pii/S0019103520303791>, doi:<https://doi.org/10.1016/j.icarus.2020.114016>.
- Pravec, P., Harris, A.W., 2000. Fast and slow rotation of asteroids. *Icarus* 148, 12–20. URL: <https://www.sciencedirect.com/science/article/pii/S0019103500964820>, doi:<https://doi.org/10.1006/icar.2000.6482>.
- Raisianzadeh, J., Mirghasemi, A.A., Mohammadi, S., 2018. 2d simulation of breakage of angular particles using combined dem and xfem. *Powder Technology* 336, 282–297. URL: <https://www.sciencedirect.com/science/article/pii/S0032591018304479>, doi:<https://doi.org/10.1016/j.powtec.2018.06.006>.
- Raisianzadeh, J., Mohammadi, S., Mirghasemi, A.A., 2019. Micromechanical study of particle breakage in 2d angular rockfill media using combined dem and xfem. *Granular Matter* 21, 48. URL: <https://doi.org/10.1007/s10035-019-0904-8>, doi:10.1007/s10035-019-0904-8.
- Reimann, J., Vicente, J., Brun, E., Ferrero, C., Gan, Y., Rack, A., 2017. X-ray tomography investigations of mono-sized sphere packing structures in cylindrical containers. *Powder Technology* 318, 471–483. URL: <https://www.sciencedirect.com/science/article/pii/S0032591017304072>, doi:<https://doi.org/10.1016/j.powtec.2017.05.033>.

- Richardson, D.C., Elankumaran, P., Sanderson, R.E., 2005. Numerical experiments with rubble piles: equilibrium shapes and spins. *Icarus* 173, 349–361. URL: <https://www.sciencedirect.com/science/article/pii/S0019103504003124>, doi:<https://doi.org/10.1016/j.icarus.2004.09.007>.
- Sánchez, P., Scheeres, D.J., 2011. SIMULATING ASTEROID RUBBLE PILES WITH A SELF-GRAVITATING SOFT-SPHERE DISTINCT ELEMENT METHOD MODEL. *The Astrophysical Journal* 727, 120. URL: <https://doi.org/10.1088/0004-637x/727/2/120>, doi:10.1088/0004-637x/727/2/120.
- Sandeep, C.S., Marzulli, V., Cafaro, F., Senetakis, K., Pöschel, T., 2019. Micromechanical behavior of dna-la lunar regolith simulants in comparison to ottawa sand. *Journal of Geophysical Research: Solid Earth* 124, 8077–8100. URL: <https://agupubs.onlinelibrary.wiley.com/doi/abs/10.1029/2019JB017589>, doi:<https://doi.org/10.1029/2019JB017589>, arXiv:<https://agupubs.onlinelibrary.wiley.com/doi/pdf/10.1029/2019JB017589>.
- Schaller, F.M., Kapfer, S.C., Evans, M.E., Hoffmann, M.J., Aste, T., Saadatfar, M., Mecke, K., Delaney, G.W., Schröder-Turk, G.E., 2013. Set voronoi diagrams of 3d assemblies of aspherical particles. *Philosophical Magazine* 93, 3993–4017. URL: <https://doi.org/10.1080/14786435.2013.834389>, doi:10.1080/14786435.2013.834389, arXiv:<https://doi.org/10.1080/14786435.2013.834389>.
- Seyyedani, S.M., Mirghasemi, A.A., Mohammadi, S., 2021. Numerical simulation of direct shear test on granular materials composed of breakable angular particles: A dem-xfem approach. *Powder Technology* 391, 450–466. URL: <https://www.sciencedirect.com/science/article/pii/S0032591021005623>, doi:<https://doi.org/10.1016/j.powtec.2021.06.038>.
- Suhr, B., Six, K., 2017. Parametrisation of a dem model for railway ballast under different load cases. *Granular Matter* 19, 64. URL: <https://doi.org/10.1007/s10035-017-0740-7>, doi:10.1007/s10035-017-0740-7.
- Sánchez, P., 2015. Asteroid evolution: Role of geotechnical properties. *Proceedings of the International Astronomical Union* 10, 111–121. doi:10.1017/S1743921315008583.
- Sánchez, P., Renouf, M., Azéma, E., Mozul, R., Dubois, F., 2021. A contact dynamics code implementation for the simulation of asteroid evolution and regolith in the asteroid environment. *Icarus* 363, 114441. URL: <https://www.sciencedirect.com/science/article/pii/S0019103521001238>, doi:<https://doi.org/10.1016/j.icarus.2021.114441>.
- Sánchez, P., Scheeres, D.J., 2014. The strength of regolith and rubble pile asteroids. *Meteoritics & Planetary Science* 49, 788–811. URL: <https://onlinelibrary.wiley.com/doi/abs/10.1111/maps.12293>, doi:<https://doi.org/10.1111/maps.12293>, arXiv:<https://onlinelibrary.wiley.com/doi/pdf/10.1111/maps.12293>.
- Thuillet, Florian, Michel, Patrick, Maurel, Clara, Ballouz, Ronald-Louis, Zhang, Yun, Richardson, Derek C., Biele, Jens, Tatsumi, Eri, Sugita, Seiji, 2018. Numerical modeling of lander interaction with a low-gravity asteroid regolith surface - application to mascot on board hayabusa2. *A&A* 615, A41. URL: <https://doi.org/10.1051/0004-6361/201832779>, doi:10.1051/0004-6361/201832779.
- Thuillet, Florian, Zhang, Yun, Michel, Patrick, Biele, Jens, Kameda, Shingo, Sugita, Seiji, Tatsumi, Eri, Schwartz, Stephen R., Ballouz, Ronald-Louis, 2021. Numerical modeling of lander interaction with a low-gravity asteroid regolith surface - ii. interpreting the successful landing of hayabusa2 mascot. *A&A* 648, A56. URL: <https://doi.org/10.1051/0004-6361/201936128>, doi:10.1051/0004-6361/201936128.
- Tsuchiyama, A., Uesugi, M., Matsushima, T., Michikami, T., Kadono, T., Nakamura, T., Uesugi, K., Nakano, T., Sandford, S.A., Noguchi, R., Matsumoto, T., Matsuno, J., Nagano, T., Imai, Y., Takeuchi, A., Suzuki, Y., Ogami, T., Katagiri, J., Ebihara, M., Ireland, T.R., Kitajima, F., Nagao, K., Naraoka, H., Noguchi, T., Okazaki, R., Yurimoto, H., Zolensky, M.E., Mukai, T., Abe, M., Yada, T., Fujimura, A., Yoshikawa, M., Kawaguchi, J., 2011. Three-dimensional structure of hayabusa samples: Origin and evolution of itokawa regolith. *Science* 333, 1125–1128. URL: <https://www.science.org/doi/abs/10.1126/science.1207807>, doi:10.1126/science.1207807, arXiv:<https://www.science.org/doi/pdf/10.1126/science.1207807>.
- Voronoi, G., 1908. Nouvelles applications des paramètres continus à la théorie des formes quadratiques. deuxième mémoire. recherches sur les paralléloèdres primitifs. *Journal für die reine und angewandte Mathematik* 1908, 198–287.
- Walsh, K.J., 2018. Rubble pile asteroids. *Annual Review of Astronomy and Astrophysics* 56, 593–624. URL: <https://doi.org/10.1146/annurev-astro-081817-052013>, doi:10.1146/annurev-astro-081817-052013, arXiv:<https://doi.org/10.1146/annurev-astro-081817-052013>.
- Watanabe, S.i., Tsuda, Y., Yoshikawa, M., Tanaka, S., Saiki, T., Nakazawa, S., 2017. Hayabusa2 mission overview. *Space Science Reviews* 208, 3–16. URL: <https://doi.org/10.1007/s11214-017-0377-1>, doi:10.1007/s11214-017-0377-1.
- Weis, S., Schröter, M., 2017. Analyzing x-ray tomographies of granular packings. *Review of Scientific Instruments* 88, 051809. URL: <https://doi.org/10.1063/1.4983051>, doi:10.1063/1.4983051, arXiv:<https://doi.org/10.1063/1.4983051>.
- Wright, E., Quillen, A.C., Sanchez, P., Schwartz, S.R., Nakajima, M., Askari, H., Miklavcic, P., 2021. Ricochets on asteroids ii: Sensitivity of laboratory experiments of low velocity grazing impacts on substrate grain size arXiv:2109.06249.
- Wright, E., Quillen, A.C., South, J., Nelson, R.C., Sánchez, P., Siu, J., Askari, H., Nakajima, M., Schwartz, S.R., 2020. Ricochets on asteroids: Experimental study of low velocity grazing impacts into granular media. *Icarus* 351, 113963. URL: <https://www.sciencedirect.com/science/article/pii/S001910352030333X>, doi:<https://doi.org/10.1016/j.icarus.2020.113963>.
- Xu, Y., Padding, J., Kuipers, J., 2014. Numerical investigation of the vertical plunging force of a spherical intruder into a prefluidized granular bed. *Physical review. E, Statistical, nonlinear, and soft matter physics* 90, 062203–1/10.
- Yano, H., Kubota, T., Miyamoto, H., Okada, T., Scheeres, D., Takagi, Y., Yoshida, K., Abe, M., Abe, S., Barnouin-Jha, O., Fujiwara, A., Hasegawa, S., Hashimoto, T., Ishiguro, M., Kato, M., Kawaguchi, J., Mukai, T., Saito, J., Sasaki, S., Yoshikawa, M., 2006. Touchdown of the hayabusa spacecraft at the mesa sea on itokawa. *Science* 312, 1350–1353. URL: <https://www.science.org/doi/abs/10.1126/science.1126164>, doi:10.1126/science.1126164, arXiv:<https://www.science.org/doi/pdf/10.1126/science.1126164>.
- Zhang, C., Zhao, S., Zhao, J., Zhou, X., 2021. Three-dimensional voronoi analysis of realistic grain packing: An xct assisted set voronoi tessellation framework. *Powder Technology* 379, 251–264. URL: <https://www.sciencedirect.com/science/article/pii/S0032591020310032>, doi:<https://doi.org/10.1016/j.powtec.2020.10.054>.
- Zhang, Y.X., An, X.Z., Zhang, Y.L., 2015. Multi-particle fem modeling on microscopic behavior of 2d particle compaction. *Applied Physics A* 118, 1015–1021. URL: <https://doi.org/10.1007/s00339-014-8861-x>, doi:10.1007/s00339-014-8861-x.

Zhao, S., Zhang, N., Zhou, X., Zhang, L., 2017. Particle shape effects on fabric of granular random packing. *Powder Technology* 310, 175–186. URL: <https://www.sciencedirect.com/science/article/pii/S0032591016309743>, doi:<https://doi.org/10.1016/j.powtec.2016.12.094>.

5. Appendix I: Verifying the model performance

Finite element method is not often applied to model discrete grains. A primary difference between the triangular grain and a DEM spherical grain is the number of nodes per discrete element that must be managed. Spherical DEM only has one node and a fixed radius, allowing for high optimization of simulation codes and efficient algorithms for contact and friction controls. In contrast, the right triangle grains have three nodes and flat sides allowing for more complex inter-grain contact to arise. Because of this, the contact algorithms employed by Abaqus must be more versatile. This is examined using two parallel simulations. The first simulation is of an impact into a bed of spheres, modeled in Abaqus and thus dependent on Abaqus' contact algorithm. The second simulation tests the same scenario, but with the model built in LAMMPS. LAMMPS was selected as it is a widely used discrete granular systems solver. In both simulations, the impactor connects with the surface at an angle of 60° from the horizontal and a velocity of 4 m/s.

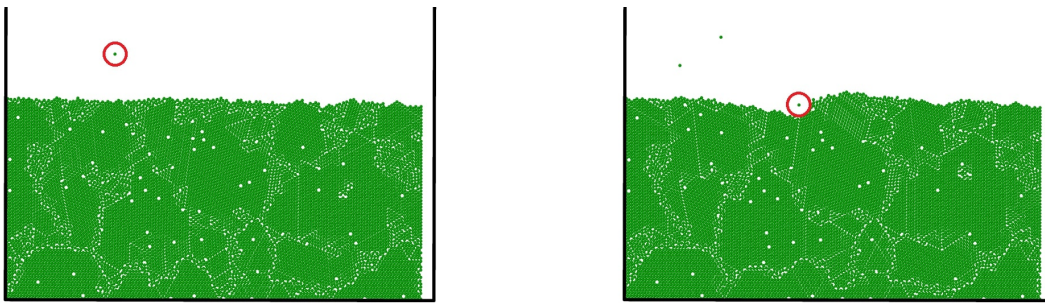


Figure 10: Initial and final frames of LAMMPS impact simulation. The particle representing the projectile is circled in red.

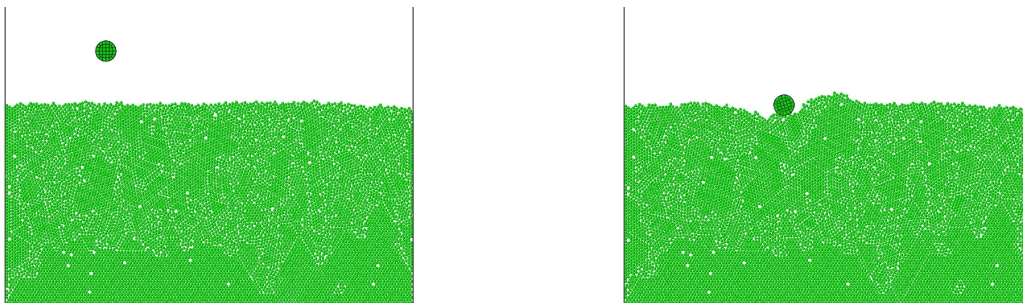


Figure 11: Initial and final frames of Abaqus impact simulation.

Figures 10 and 11 depict the initial and final frames of the impact simulations carried out in LAMMPS and Abaqus, respectively. Qualitatively, it is observed that both simulations result in a clear full-stop of the impactor. The width and depth of both craters are similar and the 'mounds' of material at the leading edges of the craters are of comparable size. Despite the minute differences in how the LAMMPS and Abaqus models are formulated in terms of material properties and contact controls, it is clear that both platforms performed similarly.

To strengthen the argument that Abaqus' contact performs similar to LAMMPS', a comparison can also be made using kinetic energy. For each simulation, the magnitude of the translational velocities of the impactor were exported and read into a script to calculate kinetic energy throughout the simulation. This approach allows dispersion of the impactor's kinetic energy to be plotted together, shown in Figure 12. The top plot shows the all kinetic energy calculated

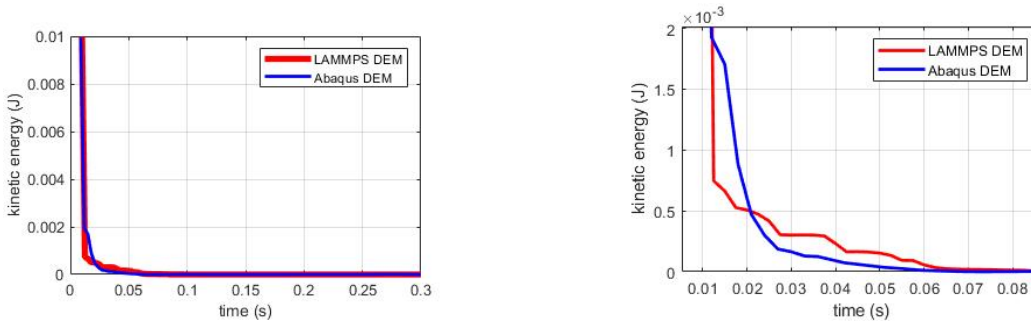


Figure 12: Plot of kinetic energy versus time for the entire simulation (top) and zoomed in (bottom).

through the simulation and the bottom plot shows the zoomed in region between 0.01s and 0.08s where most kinetic energy dispersion into the granular bed occurs. First, the slightly varied topography of each simulation is evident by the deviation of kinetic energy trends. Since the granular beds in each simulation were generated independently under gravity, the exact 'pathways' through which kinetic energy is drained are not identical during the impacts. However, in both simulations, the kinetic energy settles to zero at almost the exact same point in between 0.06s and 0.07s. This observation implies that the average rate by which kinetic energy is drained into the granular bed is very similar in both cases. Slight discrepancies noticed over the course of the dispersion are attributed to the slight difference in material property and contact definition in Abaqus and LAMMPS models. To conclude, these findings support the performance of Abaqus' contact algorithm in the discrete modeling application.

Appendix II: Additional sub-surface findings for 30° impacts

Figure 13 displays the packing fraction density plots and Figure 14 shows the Von Mises strain contours for 30° impacts ranging from 2 m/s to 10 m/s. Because most of these impact events are ricochets, there is lesser ejecta spread across the surface than for impacts at 60°. The shallower impact angle also produces greater asymmetry in both the packing fraction and strain analysis results.

For 30° impacts, the trend in growth of the skin zone is more straightforward than for 60°. This is demonstrated in the smoothed data for 30° impacts in Figure 8a, where the maximum skin depth and width of the skin zone increase continually with increasing velocity.

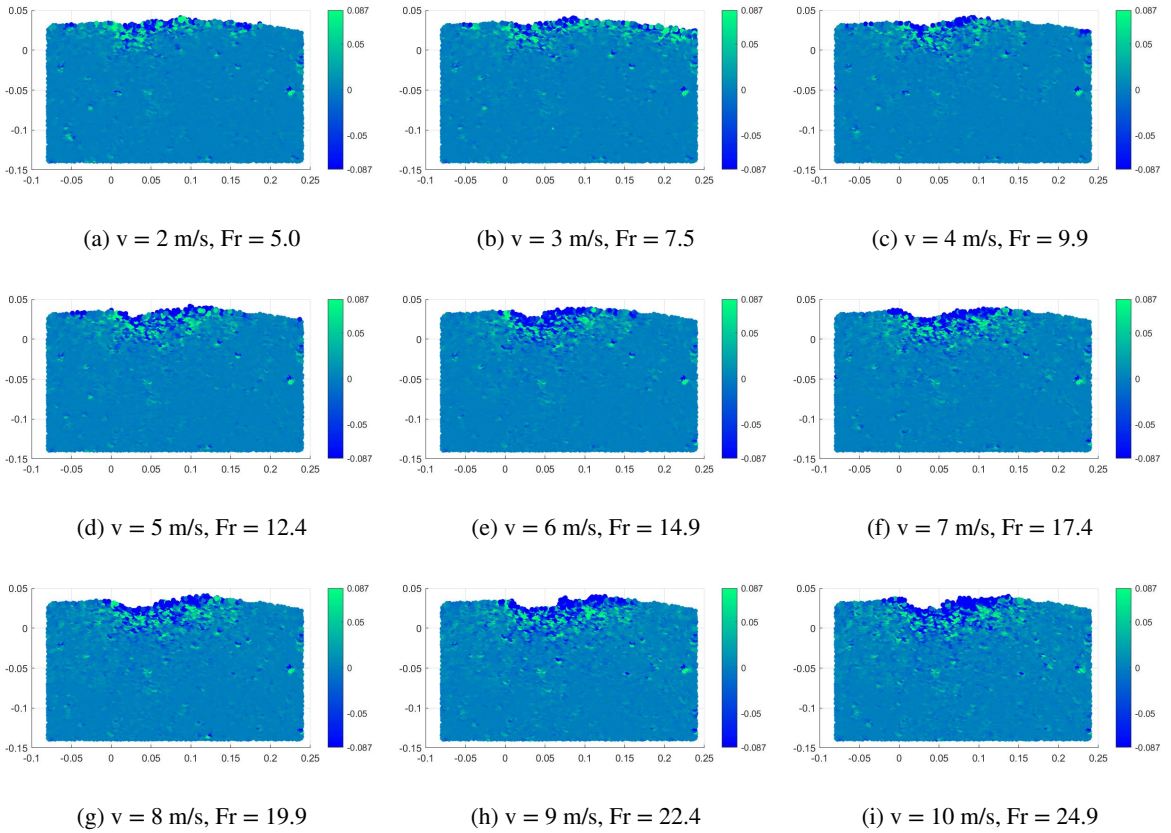


Figure 13: Colored packing density plots illustrating results for 30° impacts

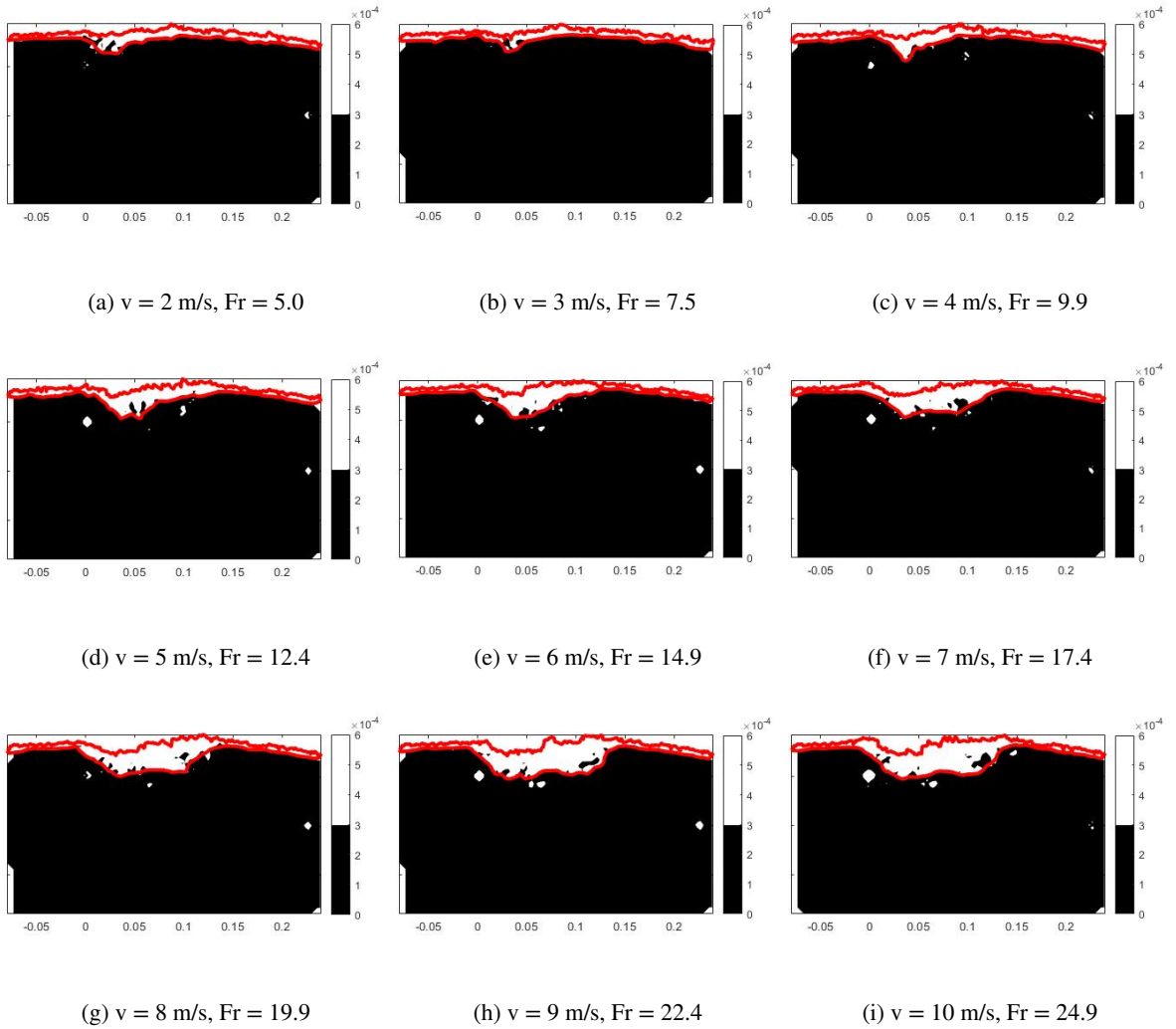


Figure 14: Contour plots of Von Mises strain distribution for 30° impacts